GSA Data Repository 2017244

Cryptic metasomatism during late-stage lunar magmatism implicated by sulfur in apatite

Brian A. Konecke[1], Adrian Fiege[1, 2], Adam C. Simon[1], and Francois Holtz[3]

GSA Data Repository item 201Xxxx, [Modeling and experimental methods (DR1); data tables (DR2); extended discussion (DR3); DR Figures 3.1 and 3.2], is available online at www.geosociety.org/pubs/ft20XX.htm, or on request from editing@geosociety.org or Documents Secretary, GSA, P.O. Box 9140, Boulder, CO 80301, USA.

Data Repository (DR)1. Methods

DR1.1 Experimental approach

Gold capsules (3.8 mm O.D., 0.12 mm wall thickness, 10 mm length) were loaded stepwise with ~37 mg of anhydrous rhyolitic or lamproitic glass (DR Table 2.1), ~3 μL H_2O (or ~1.8 μL H_2O for the ΔFMQ-1 experiment), and either: 0.2, 0.4, or 0.8 mg pyrrhotite. The elevated water contents (>4 wt.%) are required to promote crystal growth; however, as mentioned in the main text, the results are applicable to lunar magmas and allow us evaluate the S signature in apatite from lunar mare basalts. The capsules were weighed, welded shut, and placed in a drying oven (110-120°C) for several hours, then re-weighed to check for water loss. Charges were pressurized to ~100 MPa and rapidly decompressed to confirm the mechanical integrity of the welds and capsule. Apatite crystallization experiments were run at 1,000°C and 300 MPa for 3-5 days at the oxygen fugacity (fO_2) values of ΔFMQ-1, ΔFMQ and ΔFMQ+3, where FMQ is the fayalite-magnetite-quartz oxygen fugacity buffer. The fO_2 was controlled by adding H_2 to the Ar-pressure medium and was monitored by using a Shaw-membrane (Berndt et al., 2002). We highlight that ΔFMQ-1 is the lowest fO_2 conditions that can feasibly be achieved in the IHPV

apparatus used in this study at 300 MPa, 1,000°C, and >4 wt% H_2O. After rapid quench (Berndt et al., 2002): (a) the capsules were re-weighed to confirm their mechanical integrity at run conditions, and (b) the run products were then carefully recovered from the capsules. Capsules revealing loss of weight (i.e., of volatiles/water) during any of the experimental steps were discarded. Mafic experiments were performed to test the melt compositional effect on S partitioning between apatite and melt, but are of lower importance for this study as discussed below (DR Section 3.1); note: the mafic sulfide saturated experiment was performed Konecke et al. (2017). The compositions of the (anhydrous) starting glasses are provided in DR Table 2.1.

All experiments produced a homogenous glass and un-zoned, coexisting apatite grains >5 um in diameter. The presence of sulfides (or sulfates) within the nominally sulfide (or sulfate) saturated runs was confirmed via energy dispersive spectroscopy (EDS). The lamproite runs are characterized by a high crystallinity with clinopyroxene (cpx), amphibole (amp), and ± iron sulfide (po; e.g., depending on the fO_2 of the system) as mineral phases in addition to apatite; mineral phases identified via EDS. The analytical results of the felsic and mafic apatite crystallization experiments are provided in DR Table 2.2 and 2.3.

DR1.2 Electron probe microanalysis (EPMA) and Fourier transform infrared (FTIR) spectroscopy

The experimental run products (glass and apatite) and natural apatite from the terrestrial Carmen iron oxide – apatite ore deposit, Chile, were characterized quantitatively by wavelength dispersive electron probe microanalysis (EPMA) by using a CAMECA SX-100 at the University of Michigan (UM), American Museum of Natural History (AMNH), and at the Leibniz University Hannover (LUH). An acceleration voltage of 15 keV, a beam current of 10 nA and a beam size of 2 μm was used for all element analysis of apatite (except for S); a second beam condition (15 keV, 35 nA, ~1-2 μm beam) was used for S to achieve limits of detection of ~30 μg/g S. Counting times for the apatite analyses were: 5 s for F; 20 s for Cl; and 240 s for S. An

acceleration voltage of 15 keV, a beam current of 5-10 nA and a beam size of 5-10 μm beam was used for EPMA of the glasses. Counting times for the glass analyses were: 10 s for F; 20 s for Cl; and 240 s for S. Precautions were taken to prevent beam damage of glass (e.g., Cl, Na diffusion and Al, Si burn-in) and apatite (e.g., F migration owing to crystallographic orientation effects; Goldoff et al., 2012) during EPMA. Monitoring of Durango apatite (a fluorapatite) during the EPMA sessions confirmed the suitability of our analytical approach for high-precision apatite analysis (e.g., the F content was reproduced within ~5 % relative to the known content in Durango apatite; cf. Jarosewich et al. 1980). Both SiO_2 and Al_2O_3 concentrations were monitored in experimental apatites to determine possible contribution from the surrounding glass and mineral assemblages.

Fourier transform infrared (FTIR) spectroscopy was performed at the American Museum of Natural History (AMNH) to quantify the water content of experimental rhyolitic glasses (mafic glass pockets were too small to measure with FTIR) using the instrumentation and methods described by Mandeville et al. (2002), and using the molar absorption coefficients of Ohlhorst et al. (2001). The H_2O contents measured via FTIR were within analytical error of the contents estimated from mass balance calculations (see SI Table 2.2).

DR 2. Supplementary Tables

DR Table 2.1: Starting glass compositions

DR Table 2.2: EPMA of experimental apatite and felsic (AP1008-IH) glass

DR Table 2.3: EPMA of experimental apatite and mafic (LA45-IH) glass

DR Table 2.4: EPMA of Mina Carmen apatite

Data Repository Table DR2.1: Starting glass compositions

wt.%	SiO_2	TiO_2	Al_2O_3	FeO	MnO	MgO	CaO	Na_2O	K_2O	P_2O_5	H_2O	F	Total
Felsic (*AP1008)	72.83	0.05	13.68	1.12	0.01	0.17	2.21	3.30	4.55	1.47	n.d.	0.14	99.53
Mafic (**LA45)	40.13	4.37	8.57	8.75	0.20	9.21	16.24	0.50	5.29	3.81	n.d.	n.d.	97.07

Notes: *AP1008: Granite from the Krůsné Hory Mts. (Erzhebirge, Europe) + 3 Wt.% P_2O_5; fused at 1,500°C for 3 hr.

**LA45: Lamproite (sample AL/KB6-98) from Luttinen et al. (2002); Loss of ignition (LOI) at 1,200°C = 8.40%.
Felsic glass analyzed by EPMA at UM; mafic glass by XRF at LUH; n.d. not detected

Table DR2.2: EMPA of experimental AP1008-IH apatites & glass

	AP1008-IH1	AP1008-IH1	AP1008-IH2	AP1008-IH2	AP1008-IH24	AP1008-IH24	AP1008-IH17	AP1008-IH17
	Ap	Glass	Ap	Glass	Ap	Glass	Ap	Glass
wt.%	Sulfide saturated		Sulfide undersaturated		Sulfide saturated		Sulfate saturated	
SiO_2	1.03 ±0.20	68.58 ±0.13	0.75 ±0.15	68.43 ±0.16	0.88 ±0.17	71.44 ±0.20	0.40 ±0.08	69.15 ±0.31
Al_2O_3	0.21 ±0.05	12.74 ±0.03	0.15 ±0.03	12.68 ±0.05	0.14 ±0.04	13.69 ±0.20	0.05 ±0.03	13.36 ±0.06
FeO	0.69 ±0.01	1.17 ±0.02	0.67 ±0.03	1.31 ±0.03	0.74 ±0.02	1.18 ±0.03	0.48 ±0.01	1.75 ±0.03
MgO	0.19 ±0.01	0.16 ±0.00	0.18 ±0.01	0.16 ±0.00	0.21 ±0.01	0.17 ±0.01	0.19 ±0.01	0.17 ±0.01
MnO	0.15 ±0.01	b.d.	0.16 ±0.01	b.d.	0.17 ±0.01	0.05 ±0.01	0.16 ±0.01	0.05 ±0.01
CaO	52.16 ±0.30	1.83 ±0.08	52.71 ±0.28	1.81 ±0.13	53.02 ±0.28	1.26 ±0.02	53.21 ±0.10	1.39 ±0.01
K_2O	0.21 ±0.01	4.18 ±0.02	0.20 ±0.02	4.17 ±0.02	0.18 ±0.01	3.97 ±0.03	0.14 ±0.01	3.51 ±0.18
Na_2O	0.18 ±0.02	2.86 ±0.01	0.17 ±0.03	2.64 ±0.03	0.15 ±0.01	2.78 ±0.05	0.18 ±0.01	1.82 ±0.15
P_2O_5	41.40 ±0.12	1.16 ±0.06	41.28 ±0.25	1.21 ±0.10	41.10 ±0.18	0.76 ±0.02	41.60 ±0.19	0.91 ±0.02
Ce_2O_3	0.43 ±0.02	b.d.	0.43 ±0.01	b.d.	0.37 ±0.03	b.d.	0.32 ±0.01	b.d.
La_2O_3	0.27 ±0.01	b.d.	0.21 ±0.02	b.d.	0.27 ±0.03	b.d.	0.19 ±0.01	b.d.
Cl	0.12 ±0.00	b.d.	0.10 ±0.00	b.d.	0.01 ±0.01	b.d.	0.01 ±0.01	b.d.
F	2.16 ±0.03	b.d.	2.15 ±0.11	b.d.	1.82 ±0.01	b.d.	2.00 ±0.06	b.d.
SO_3	0.02 ±0.00	0.05 ±0.00	0.01 ±0.00	0.05 ±0.00	0.02 ±0.00	0.05 ±0.00	0.14 ±0.01	0.10 ±0.00
O=F, Cl	0.94	-	0.93	-	0.77	-	0.84	-
OH wt.%	1.36*	-	1.37*	-	1.71*	-	1.54*	-
Mass Balance H_2O	-	7.29 ±0.11	-	7.56 ±0.10	-	4.55 ±0.23	-	7.38 ±0.17
FTIR	-	7.69 ±0.31	-	7.59 ±0.31	-	n.a.	-	n.a.
Total	99.64 ±0.34	92.73 ±0.11	99.61 ±0.35	92.46 ±0.10	100.05 ±0.32	92.46 ±0.10	99.75 ±0.09	92.49 ±0.17
S (µg/g)	88 ±8	193 ±8	33 ±5	176 ±9	84 ±21	220 ±7	571 ±46	405 ±5
# of analyses	6	15	5	18	6	10	5	19
T°C	1000		1000		1000		1000	
P (MPa)	300		300		300		300	
ΔFMQ	0		0		-1		3	
Pyrrhotite (wt.%)	1.00		0.50		2.00		1.00**	

Run Duration (hrs)	72.33	72.33	111.25	150.08
$D_S^{ap/m}$	**0.46 ±0.04**	**0.18 ±0.03**	**0.38 ±0.09**	**1.41 ±0.11**

Notes: b.d. is below detection limit; n.a. is not analyzed

O=F, Cl is correction factor

*Calculated using Ketcham (2015)

**~0.35 wt.% S (elemental) + ~0.92 wt.% Fe_2O_3, where the Fe/S ratio corresponds to po.

Analyses reported in 1σ standard error of mean

$D_S^{ap/m}$ reported in 1σ standard error of mean

DR Table 2.3: EMPA of experimental LA45-IH apatites & glass

wt.%	LA45-IH1* Ap	LA45-IH1* Glass	LA45-IH3 Ap	LA45-IH3 Glass
	Sulfide saturated		Sulfide undersaturated	
SiO_2	1.73 ±0.22	43.50 ±0.22	1.15 ±0.09	44.44 ±0.36
TiO_2	0.04 ±0.01	2.64 ±0.05	0.04 ±0.01	2.71 ±0.03
Al_2O_3	0.47 ±0.28	12.71±0.17	0.10 ±0.02	12.91 ±0.15
FeO	0.59 ±0.06	9.30 ±0.17	0.46 ±0.02	9.37 ±0.13
MgO	0.25 ±0.11	1.68 ±0.10	0.24 ±0.06	1.78 ±0.03
MnO	b.d.	0.30 ±0.02	b.d.	0.35 ±0.02
CaO	53.00 ±0.32	9.00 ±0.23	53.52 ±0.12	8.74 ±0.15
K_2O	0.29 ±0.03	8.93 ±0.04	0.26 ±0.02	8.39 ±0.46
Na_2O	0.01 ±0.01	1.58 ±0.04	b.d.	1.42 ± 0.08
P_2O_5	39.30 ±0.17	0.91 ±0.22	40.43 ±0.10	0.66 ±0.19
Ce_2O_3	0.54 ±0.02	b.d.	0.48 ±0.02	b.d.
La_2O_3	0.23 ±0.01	b.d.	0.22 ±0.01	b.d.
F	1.43 ±0.05	0.39 ±0.11	1.56 ±0.04	0.45 ±0.08
Cl	b.d.	0.01 ±0.01	b.d.	b.d.
SO_3	0.08 ±0.01	0.64 ±0.05	0.04 ±0.01	0.32 ±0.01
SrO	0.94 ±0.02	n.a.	1.01 ±0.04	n.a.
BaO	0.02 ±0.01	0.50 ±0.04	0.02 ±0.01	0.52 ±0.04
O=F, Cl	0.60	-	0.65	-
OH wt.%	1.93**	-	1.95**	-
Mass Balance H_2O	-	7.92 ±0.26	-	7.95 ±0.51
Total	100.25 ±0.26	92.08 ±0.26	100.79 ±0.19	92.05 ±0.51
S (µg/g)	322 ±44	2553 ±200	164 ±49	1270 ±47
# of analyses	10	7	9	8
T°C	1000		1000	
P (MPa)	300		300	
ΔFMQ	0		0	
Pyrrhotite (wt.%)	1.00		0.50	
Run Duration (hrs)	120.65		120.65	
$D_S^{ap/m}$	**0.13 ±0.02**		**0.13 ±0.04**	

Notes: b.d. is below detection limit; n.a. is not analyzed
O=F, Cl is correction factor
Data from Konecke et al. (2017)
*Calculated using Ketcham (2015)
Analyses reported in 1σ standard error of mean
$D_S^{ap/m}$ reported in 1σ standard error of mean

DR Table 2.4: EPMA of Mina Carmen apatite (data from Konecke et al., 2017)

Distance (μm) from cavity rim*	25	20	15	10	5	0	Average	l.o.d
SiO_2	b.d.	b.d.	b.d.	0.17	0.14	0.12	0.07 ±0.03	0.05
TiO_2	b.d.	b.d.	b.d.	b.d.	b.d.	b.d.	b.d.	0.02
Al_2O_3	b.d.	b.d.	b.d.	b.d.	b.d.	0.17	0.03 ±0.03	0.04
FeO	b.d.	b.d.	b.d.	b.d.	b.d.	b.d.	b.d.	0.07
MgO	b.d.	b.d.	b.d.	b.d.	b.d.	b.d.	b.d.	0.03
MnO	b.d.	b.d.	b.d.	b.d.	b.d.	b.d.	b.d.	0.07
CaO	54.87	54.97	54.89	54.34	54.21	53.55	54.47 ±0.23	0.08
K_2O	b.d.	b.d.	b.d.	b.d.	b.d.	0.09	0.01 ±0.01	0.04
Na_2O	b.d.	b.d.	b.d.	0.11	0.19	0.21	0.08 ±0.04	0.04
P_2O_5	42.17	41.89	42.10	41.17	40.44	40.41	41.37 ±0.33	0.19
Ce_2O_3	b.d.	b.d.	b.d.	b.d.	b.d.	b.d.	b.d.	0.1
La_2O_3	b.d.	b.d.	b.d.	b.d.	b.d.	b.d.	b.d.	0.12
F	3.71	3.70	3.72	3.92	1.62	2.18	3.14 ±0.40	0.51
Cl	0.25	0.20	0.29	0.49	2.60	2.33	1.03 ±0.46	0.02
SO_3	b.d.	b.d.	0.09	0.26	0.52	0.44	0.22 ±0.09	0.01
SrO	b.d.	0.01	b.d.	0.02	b.d.	b.d.	b.d.	0.14
BaO	b.d.	0.08	0.03	b.d.	b.d.	b.d.	0.02 ±0.01	0.13
O=F, Cl	1.62	1.60	1.63	1.76	1.27	1.44	1.55 ±0.07	-
Total	99.39	99.25	99.47	98.67	98.36	97.97	98.85 ±0.25	0.25
S (μg/g)	b.d.	b.d.	347	1057	2096	1764	877 ±370	-

Notes: b.d. is below detection limit; data reported in wt.% unless otherwise noted; l.o.d is limit of detection (elemental %)

*EPMA transect started approximately ±10-15 um from rim

Error reported in 1σ standard error of mean

DR 3. Extended discussion

DR 3.1 Fractional Crystallization of Mafic Melt Scenario

In addition to the scenarios discussed in the main text, an empirically testable hypothesis invokes early crystallization of lunar apatite from a mafic silicate melt. As for the lunar rhyolitic system, we followed Liu et al. (2007) to calculate the theoretical SCSS for mare basalt 12039 (Rhodes et a., 1977) using the following parameters: $T_{Solidus}$= 1,100°C (see main text for discussion; c.f. Taylor et al., 1991 and references therein); H_2O contents ranging from 1-100 µg/g H_2O, fO_2 of ΔIW iron-wüstite = -1 to +4, and 0.1 MPa. The model results coupled with the experimental $D_S^{ap/m}$ values (DR Table 2.3) suggest that the low S contents reported for the core of the lunar apatite (<200 µg/g; Greenwood et al., 2011; Boyce et al., 2014) are consistent with crystallization of apatite from a H_2O poor (~10 µg/g H_2O), S rich mafic melt (~1,200 µg/g S). However, this scenario for the apatite core is highly unlikely considering the low P_2O_5 content in the bulk mare basalt (~900 µg/g P_2O_5; Rhodes et al., 1977), where apatite saturation is only achieved once the residual melt in the mare basalt reached a rhyolitic composition (≥88% crystallization; Sha, 2000). Furthermore, crystallization of apatite containing ~430 µg/g S (i.e., rims of lunar apatite) would require an implausible amount of ~3,300 µg/g S in a H_2O poor (~10 µg/g H_2O) mafic melt.

DR3.2 Volatile signatures in terrestrial and extraterrestrial apatite

An alternative approach to decipher the lunar apatite volatile signatures is to compare them with the volatile signature systematics of terrestrial apatite. Apatite from iron oxide-apatite (IOA) ore deposits—which occur globally and are produced by magmatic-hydrothermal processes in volcanic systems (Knipping et al., 2015)—fingerprint textural and chemical reactions related to metasomatism (Treloar and Colley, 1996; Harlov, 2015; DR Figure 1 and 2).

Similar F-Cl-(H)-S trends (DR Figure 1) and textural observations (e.g., volatile pathways; Nadeau et al., 2010) observed for lunar apatite and terrestrial Mina Carmen apatite perhaps reflect similar mechanisms; e.g., a metasomatic (i.e., modal and/or cryptic) reaction of fluorapatite to fluor-chlorapatite via replacement of F by Cl in the apatite structure (DR Figure 2). We stress that despite the difference in the core-to-rim length scales of volatile concentrations in terrestrial Mina Carmen apatite and lunar apatite, the similarities with respect to the overall trends, and not the absolute concentrations, can be used to infer that similar processes affected the apatite in both systems (e.g., length scales can differ depending on T-X of the volatile phase and duration of exposure).

Secondary REE-phosphate (e.g., monazite; $[Ce,LREE,Th]PO_4$) inclusions in apatites from the Mina Carmen IOA deposit (Treloar and Colley, 1996) in the Chilean iron belt evince chemical alteration via metasomatism (Harlov et al., 2015; this study). Volatile trends for F and Cl from the Mina Carmen and lunar apatite (DR Figure 1) record the reaction of fluorapatite to fluor-chlorapatite (DR Figure 1) via replacement of F by Cl in the apatite structure. Fluorapatite to chlorapatite metasomatic alteration (e.g., where $ap\text{-}X_{Cl} > ap\text{-}X_F$) via $CaCl_2$-rich brines has been observed in nepheline-bearing clinopyroxenites from the Ural Mountains, Russia; Krause et al., 2013). Similarly, extraterrestrial basalts (e.g., lunar basalts) that show evidence of metasomatism tend to contain relatively more Cl enriched apatites than non-metasomatized basalts (Hovis and Harlov, 2010; McCubbin et al., 2011; McCubbin and Jones, 2015).

High-contrast backscattered electron (BSE) images of 12039,42 apatite grain 9 (DR Figure 2A) in the study by Greenwood et al. (2011) provide evidence for complex chemical zoning in lunar apatites (e.g., heterogeneous concentrations of volatiles and rare-earth elements such as Ce). Lunar apatites from the Greenwood et al. (2011) and Boyce et al. (2014) studies show evidence of incompatible element enrichment near the rims and along cracks (fractures) within the apatite grain.

Some results reported by Greenwood et al. (2011) for lunar apatite were interpreted by the authors as being a cross-axial heterogeneity zoning effect, and excluded from further considerations (open circles in Figure 1). However, the BSE image of apatite 12039,42 grain 12 from Greenwood et al. (2011) shows that the analytical spots represented by the open circles are adjacent to cracks in the apatite crystal that are bordered by incompatible element enrichment. These analytical spots are consistent with F-Cl-OH-S concentrations measured near the apatite rims, further suggesting that the volatiles signatures were induced by metasomatic alteration, post apatite crystallization.

In terrestrial volcanic systems, Nadeau et al. (2010) reported petrographic evidence for the exsolution of an aqueous phase that could produce sufficient overpressure-induced hydrofracturing and create pathways for fluid mobility upon decompression of an ascending magma. This indicates that the incompatible element enrichment of the lunar apatite rim and proximal to cracks (i.e., fluid pathways) within apatite may have formed after the formation of the apatite core, since the pathways crosscut the preexisting core of the apatite grains (see DR Figure 3.2).

Similar fluid pathways are observed in apatite from the terrestrial Carmen deposit, where fluid infiltration and alteration is evidenced by the presence of REE-phosphate inclusions (e.g., monazite; (Ce,LREE,Th)(PO_4); see DR Figure 3.2). Formation of nano- and micro-porosity in metasomatically altered regions of apatite enhances fluid permeation, which promotes rapid diffusive mass transfer of cations and anions between the fluid and the apatite (Harlov et al., 2005; Kusebauch et al., 2015). The presence of REE-phosphate inclusions in Carmen apatite provides further evidence that the porosity (e.g., fluid pathways; see DR Figure 2) was sufficient enough to allow fluid-induced dissolution and re-precipitation of REE-phosphates. However, hydrothermal fluids containing aqueous Na (e.g., NaCl brines) discourage the dissolution-reprecipitation of REE-phosphate inclusions, since Na is less prone to leave the apatite structure

because charge balance is retained (Harlov et al., 2015), and plausibly explains the absence of REE-phosphates adjacent to lunar apatite 12039,42.

The similar trends observed for F, Cl and S (Figure DR1) indicate an incorporation of S on the column anions site of apatite, consistent with Konecke et al. (2017) and also indicating similar processes. Finally, although probably less likely, the volatile signatures in both Carmen and lunar apatite could also be explained by dissolution and reprecipitation reactions of the apatite in the presence of a metasomatic fluid (e.g., Engvik et al., 2009).

DR3.3 Absence of glass alteration

EPMA of the evolved glass believed to be in equilibrium with lunar apatite 12039,42 (Greenwood et al., 2011; Boyce et al., 2014) revealed exceedingly low S-content (e.g., below a reasonable limit of detection of <100 μg/g S for the reported EPMA conditions). Thus, as discussed above and in the main text, we argue that the volatile signature in lunar apatite is related to metasomatism in the presence of a free volatile phase. Our observations and interpretations beg the question as to why the apatite exhibits evidence of hydrothermal alteration, whereas the evolved and late-stage glass does not. A first order explanation is provided by the fact that glass analyses are often performed near the center of the glass using, e.g., a defocused ion/electron beam (typically 5 to 20 μm; i.e., relatively low spatial resolution) in order to avoid contribution from surrounding mineral assemblages, while minimizing the impact on the sample (e.g., Na migration, see Devine et al., 1995). However, the consequence of this technique is that it cannot yield much chemical information regarding the edge or rim of the glass. In other words, if the element diffusion length scales into the glass are short, the interaction volume of the probe will not detect elevated S-concentrations.

We further suggest that the lack of alteration signatures in the residual glass of 12039 lunar mare basalt is directly related to the high fluid-melt partition coefficients for S (especially in reduced systems; Zajacz et al., 2012), as well as due to a kinetically sluggish uptake of S by the

evolved felsic lunar glass when compared to the apatite. In relatively more oxidizing systems (unrealistic for lunar magmas), where anhydrite ($CaSO_4$) is the predominant S-bearing phase, tephra can sequester S (e.g., specifically SO_2) at T > 600°C (Aryis et al., 2013). The scavenging ability of tephra is controlled by the rate at which Ca^{2+} diffuses towards the glass interface, where it forms Ca-S complexes (Aryis et al., 2013). However, at the low fO_2 of lunar systems (i.e., ~ΔFMQ-4), S^{2-} is the only relevant oxidation state of S in the melt and it most likely forms complexes with Fe^{2+} in the melt structure (Zajacz et al., 2012; Fiege et al., 2015). Thus, the uptake of S into the quenched residual felsic melt from a hydrothermal fluid is presumably controlled by Fe diffusion. In turn, the low Fe contents in the residual lunar melt (<0.3 wt.% FeO) will further limit the potential uptake of S explaining the sluggish (not detected) uptake of S by the residual felsic glass in the mare basalts when compared to apatite.

Alternatively, as briefly discussed in the main text, the lunar apatite signatures could reflect high water concentrations in a residual felsic melt of the lunar mare basalts (>>10,000 μg/g H_2O), where the residual melt degassed after apatite formation and solidifies soon after; i.e. the apatite has no time to re-equilibrate. Although there is some recent evidence for elevated water contents in some lunar rhyolites (Mills et al., 2017), the absence of vesicles in the lunar mare basalt contradicts this scenario.

DR3.4 Stable Isotope Systematics

Previous studies have used stable isotope systematics to investigate degassing of lunar magmas (cf. McCubbin et al., 2015B, and references therein). Recently, it has been demonstrated that the applicability of Cl isotopes to the "water-on-moon-debate" remains controversial (Ustunisik et al., 2015). Boyce et al. (2015) propose early degassing of the Moon's magma ocean; such degassing may "alter" the signature in lunar apatite (in particular those samples closer to the surface that were collected during the Apollo missions), consistent with the cryptic metasomatism hypothesis proposed in this study for apatite in lunar mare basalt (see main text).

DR4. Brief petrographic description

DR4.1 Mina Carmen

The Mina Carmen iron oxide apatite (IOA) deposit is located ~20 km E of the Atacama fault system in northern Chile (26.346993°S; 70.143110°W). The deposit is hosted within porphyritic andesite of the Los Cerros Florida formation and is dominated by massive iron oxide ore bodies consisting of magnetite and patches of modally minor hematite and minor apatite (Treloar and Colley, 1996). Apatite occurs as coarse-grained crystals up to 50 cm in length within the magnetite matrix and also within planar zones of magnetite. Halogen (F, Cl) and volatile (S) element zonation observed in Carmen apatite (Treloar and Colley, 1996; Konecke et al., 2017) is interpreted to represent primary magmatic fluorapatite that was subsequently metasomatically overprinted to chlorapatite (ap-X_{Cl} > ap-X_F) by an aqueous Cl-S-rich, F-poor phase.

DR4.2 Apollo 12 low Ti-mare basalt 12039

Lunar sample 12039 is characterized as pigeonite basalt containing mm-sized pyroxene, plagioclase and tridymite (Rhodes et al., 1977; Baldridge et al., 1979; Neal et al., 1994). Apatite found within the mesostasis and is interpreted to have been associated with late-stage crystallization features such as high K, Si glass, pyroxferroite and Ba-rich feldspar (Greenwood et al., 2011). Sample 12039,42 contains minor apatite that is relatively enriched in S (e.g., up to 430 μg/g S) and OH (up to ~1.1 wt% H_2O; Greenwood et al., 2011; Boyce et al., 2014).

DR References

Anand, M., Tartèse, R., and Barnes, J.J., 2014, Understanding the origin and evolution of water in the Moon through lunar sample studies.: Philosophical transactions. Series A, Mathematical, physical, and engineering sciences, v. 372, no. 2024, p. 20130254, doi: 10.1098/rsta.2013.0254.

Ayris, P.M., Lee, a. F., Wilson, K., Kueppers, U., Dingwell, D.B., and Delmelle, P., 2013, SO2 sequestration in large volcanic eruptions: High-temperature scavenging by tephra: Geochimica et Cosmochimica Acta, v. 110, p. 58–69, doi: 10.1016/j.gca.2013.02.018.

Baldridge W. S., Beaty D. W., Hill S. M. R., and Albee A., 1979, The petrology of the Apollo 12 pigeonite basalt suite. Proc. Lunar Planet. Sci. Conf. 10th, pp. 141–179.

Berndt, J., Liebske, C., Holtz, F., Freise, M., Nowak, M., Ziegenbein, D., Hurkuck, W., and Koepke, J., 2002, A combined rapid-quench and H_2-membrane setup for internally heated pressure vessels: Description and application for water solubility in basaltic melts: American Mineralogist, v. 87, no. 11-12, p. 1717–1726, doi: 10.2138/am-2002-11-1222.

Boyce, J.W., Tomlinson, S.M., McCubbin, F.M., Greenwood, J.P., and Treiman, a H., 2014, The lunar apatite paradox.: Science (New York, N.Y.), v. 344, no. 6182, p. 400–2, doi: 10.1126/science.1250398.

Boyce, J.W., Treiman, A.H., Guan, Y., Ma, C., Eiler, J.M., Gross, J., Greenwood, J.P., and Stolper, E.M., 2015, The chlorine isotope fingerprint of the lunar magma ocean: Science Advances, v. 1, no. 8, p. e1500380–e1500380, doi: 10.1126/sciadv.1500380.

Devine, J.D., Gardner, J.E., Brack, H.P., Layne, G.D., and Rutherford, M.J., 1995, Comparison of microanalytical methods for estimating H2O contents of silicic volcanic glasses: American Mineralogist, v. 80, no. 3-4, p. 319–328, doi: 10.2138/am-1995-3-413.

Engvik, A.K., Golla-Schindler, U., Berndt, J., Austrheim, H., and Putnis, A., 2009, Intragranular replacement of chlorapatite by hydroxy-fluor-apatite during metasomatism: Lithos, v. 112, no. 3–4, p. 236–246, doi: 10.1016/j.lithos.2009.02.005.

Fiege, A., Holtz, F., Behrens, H., Mandeville, C.W., Shimizu, N., Crede, L.S., and Göttlicher, J., 2015, Experimental investigation of the S and S-isotope distribution between H 2 O – S ± Cl fl uids and basaltic melts during decompression: Chemical Geology, v. 393-394, p. 36–54, doi: 10.1016/j.chemgeo.2014.11.012.

Goldoff, B., Webster, J.D., and Harlov, D.E., 2012, Characterization of fluor-chlorapatites by electron probe microanalysis with a focus on time-dependent intensity variation of halogens: American Mineralogist, v. 97, no. 7, p. 1103–1115, doi: 10.2138/am.2012.3812.

Greenwood, J.P., Itoh, S., Sakamoto, N., Warren, P., Taylor, L., and Yurimoto, H., 2011, Hydrogen isotope ratios in lunar rocks indicate delivery of cometary water to the Moon: Supplementary: Nature Geoscience, v. 4, no. 2, p. 79–82, doi: 10.1038/ngeo1050.

Harlov, D.E., 2015, Apatite: A Fingerprint for Metasomatic Processes: Elements, v. 11, no. 3, p. 171–176, doi: 10.2113/gselements.11.3.171.

Harlov, D.E., Wirth, R., and Förster, H.J., 2005, An experimental study of dissolution–reprecipitation in fluorapatite: fluid infiltration and the formation of monazite: Contributions to Mineralogy and Petrology, v. 150, no. 3, p. 268–286, doi: 10.1007/s00410-005-0017-8.

Hovis, G.L., and Harlov, D.E., 2010, Solution calorimetric investigation of fluor-chlorapatite crystalline solutions: American Mineralogist, v. 95, no. 7, p. 946–952, doi: 10.2138/am.2010.3485.

Jarosewich E.., Nelen, J.A., and Norberg, J.A., 1980, Reference samples for electron microprobe analysis: Geostandards Newsletter, v. 4, no. 1, p. 43–47.

Ketcham, R.A., 2015, Technical Note: Calculation of stoichiometry from EMP data for apatite and other phases with mixing on monovalent anion sites: American Mineralogist, v. 100, no. 7, p. 1620–1623, doi: 10.2138/am-2015-5171.

Knipping, J.L., Bilenker, L.D., Simon, A.C., Reich, M., Barra, F., Deditius, A.P., Lundstrom, C., Bindeman, I., and Munizaga, R., 2015, Giant Kiruna-type deposits form by efficient flotation of magmatic magnetite suspensions: Geology, v. 43, no. 7, p. 591–594, doi: 10.1130/G36650.1.

279 Konecke, B.A., Fiege, A., Simon, A.C., and Parat, F., 2017, Co-variability of S6+, S4+ and S2- in
280 apatite as a function of oxidation state – implications for a new oxybarometer: v. 102, p.
281 548–557, doi: http://dx.doi.org/10.2138/am-2017-5907.
282 Krause, J., Harlov, D.E., Pushkarev, E. V., and Brügmann, G.E., 2013, Apatite and clinopyroxene
283 as tracers for metasomatic processes in nepheline clinopyroxenites of Uralian-Alaskan-
284 type complexes in the Ural Mountains, Russian Federation: Geochimica et
285 Cosmochimica Acta, v. 121, p. 503–521, doi: 10.1016/j.gca.2013.06.013.
286 Kusebauch, C., John, T., Whitehouse, M.J., Klemme, S., and Putnis, A., 2015, Distribution of
287 halogens between fluid and apatite during fluid-mediated replacement processes:
288 Geochimica et Cosmochimica Acta, v. 170, p. 225–246, doi: 10.1016/j.gca.2015.08.023.
289 Luttinen, A. V., Zhang, X., and Foland, K.A., 2002, 159 Ma Kjakebeinet lamproites (Dronning
290 Maud Land, Antarctica) and their implications for Gondwana breakup processes:
291 Geological Magazine, v. 139, no. 05, p. 525–539, doi: 10.1017/S001675680200674X.
292 McCubbin, F.M., Jolliff, B.L., Nekvasil, H., Carpenter, P.K., Zeigler, R.A., Steele, A., Elardo,
293 S.M., and Lindsley, D.H., 2011, Fluorine and chlorine abundances in lunar apatite:
294 Implications for heterogeneous distributions of magmatic volatiles in the lunar interior:
295 Geochimica et Cosmochimica Acta, v. 75, no. 17, p. 5073–5093, doi:
296 10.1016/j.gca.2011.06.017.
297 McCubbin, F.M., and Jones, R.H., 2015A, Extraterrestrial Apatite: Planetary Geochemistry to
298 Astrobiology: Elements, v. 11, no. 3, p. 183–188, doi: 10.2113/gselements.11.3.183.
299 McCubbin, F.M., Kaaden, K.E. Vander, Tartèse, R., Klima, R.L., Liu, Y., Mortimer, J., Barnes,
300 J.J., Shearer, C.K., Treiman, A.H., Lawrence, D.J., Elardo, S.M., Hurley, D.M., Boyce,
301 J.W., and Anand, M., 2015B, Magmatic volatiles (H, C, N, F, S, Cl) in the lunar mantle,
302 crust, and regolith: Abundances, distributions, processes, and reservoirs: American
303 Mineralogist, v. 100, no. 8–9, p. 1668–1707, doi: 10.2138/am-2015-4934ccbyncnd.

304 Nadeau, O., Williams-Jones, A.E., and Stix, J., 2010, Sulphide magma as a source of metals in
305 arc-related magmatic hydrothermal ore fluids: Nature Geoscience, v. 3, no. 7, p. 501–
306 505, doi: 10.1038/ngeo899.
307 Ohlhorst, S., Behrens, H., and Holtz, F., 2001, Compositional dependence of molar absorptivities
308 of near-infrared OH-and H2O bands in rhyolitic to basaltic glasses: Chemical Geology, v.
309 174, no. 1–3, p. 5–20, doi: 10.1016/S0009-2541(00)00303-X.
310 Rhodes, J.M, Blanchard D.P, M.A. Dungan, J.C Brannon, Rogders, K.., 1977, Chemistry of
311 Apollo 12 mare basalts: Magma types and fractionation processes: Proc. Lunar Sci. Conf.
312 8th, p. 1305–1338.
313 Stormer, J.C., Pierson, M.L., and Tackler, R.C., 1993, Variation of F and Cl X-ray intensity due
314 to anisotropic diffusion in apatite during electron microprobe analysis: American
315 Mineralogist, v. 78, p. 641–648.
316 Taylor G. J., Warren P., Ryder G., Delano J., Pieters C. and Lofgren G.,1991, Chapter 6: Lunar
317 Rocks. In Lunar Sourcebook: A User's Guide to the Moon, pp. 183–284. Cambridge
318 University Press, Cambridge, U.K.
319 Treloar, P.J., and Colley, H., 1996, Variation in F and Cl contents in apatites from magnetite-
320 apatite ores in northern Chile, and their ore-genetic implications: Mineralogical
321 Magazine, v. 60, no. April, p. 285–301.
322 Ustunisik, G., Nekvasil, H., Lindsley, D.H., and McCubbin, F.M., 2015, Degassing pathways of
323 Cl-, F-, H-, and S-bearing magmas near the lunar surface: Implications for the
324 composition and Cl isotopic values of lunar apatite: American Mineralogist, v. 100, p.
325 1717–1727, doi: http://dx.doi.org/10.2138/am-2015-4883.
326 Zajacz, Z., Candela, P. A., Piccoli, P.M., Wälle, M., and Sanchez-Valle, C., 2012, Gold and
327 copper in volatile saturated mafic to intermediate magmas: Solubilities, partitioning, and
328 implications for ore deposit formation: Geochimica et Cosmochimica Acta, v. 91, p. 140–
329 159, doi: 10.1016/j.gca.2012.05.033.

Figure DR1 A-B:

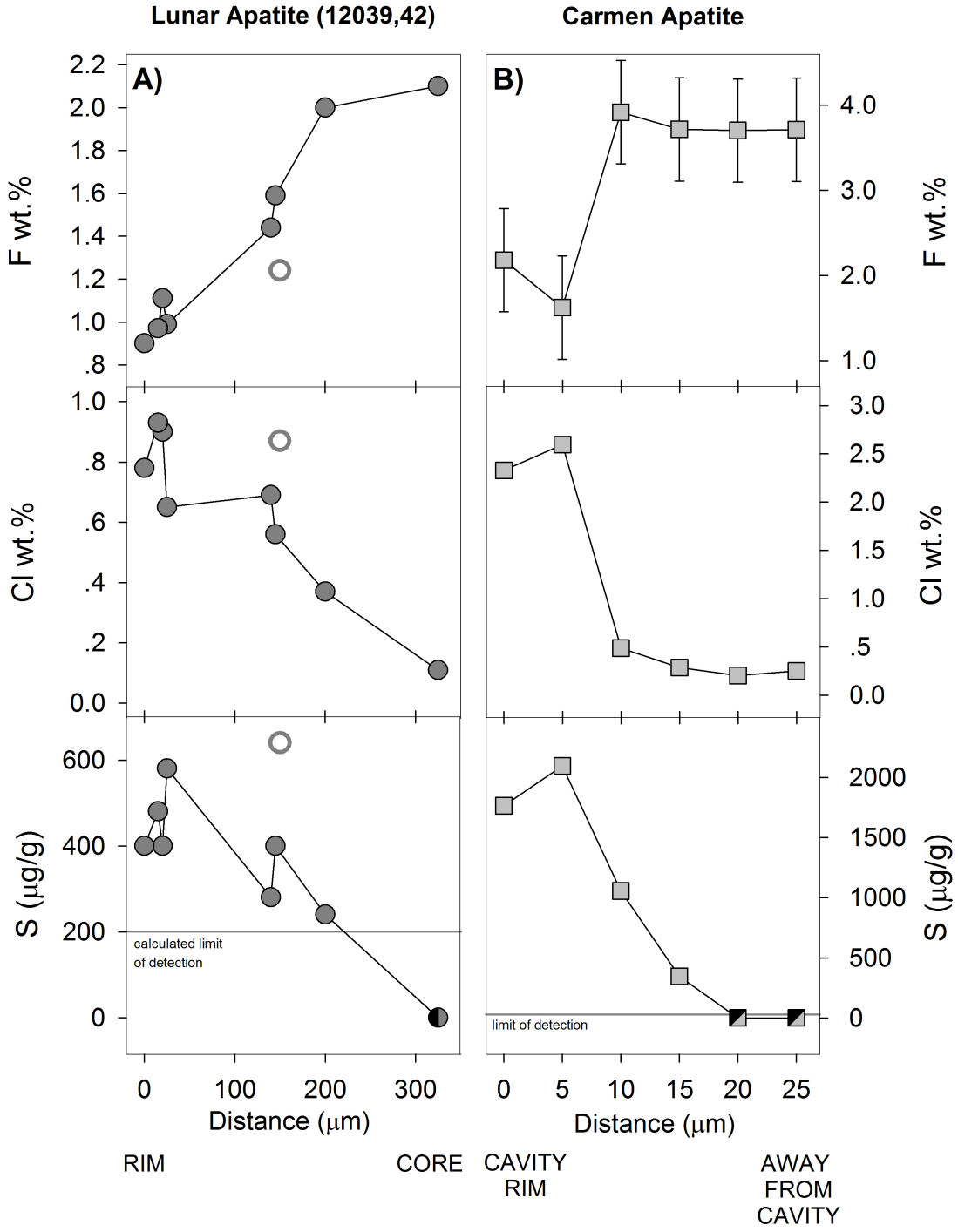

Figure DR2 A-B:

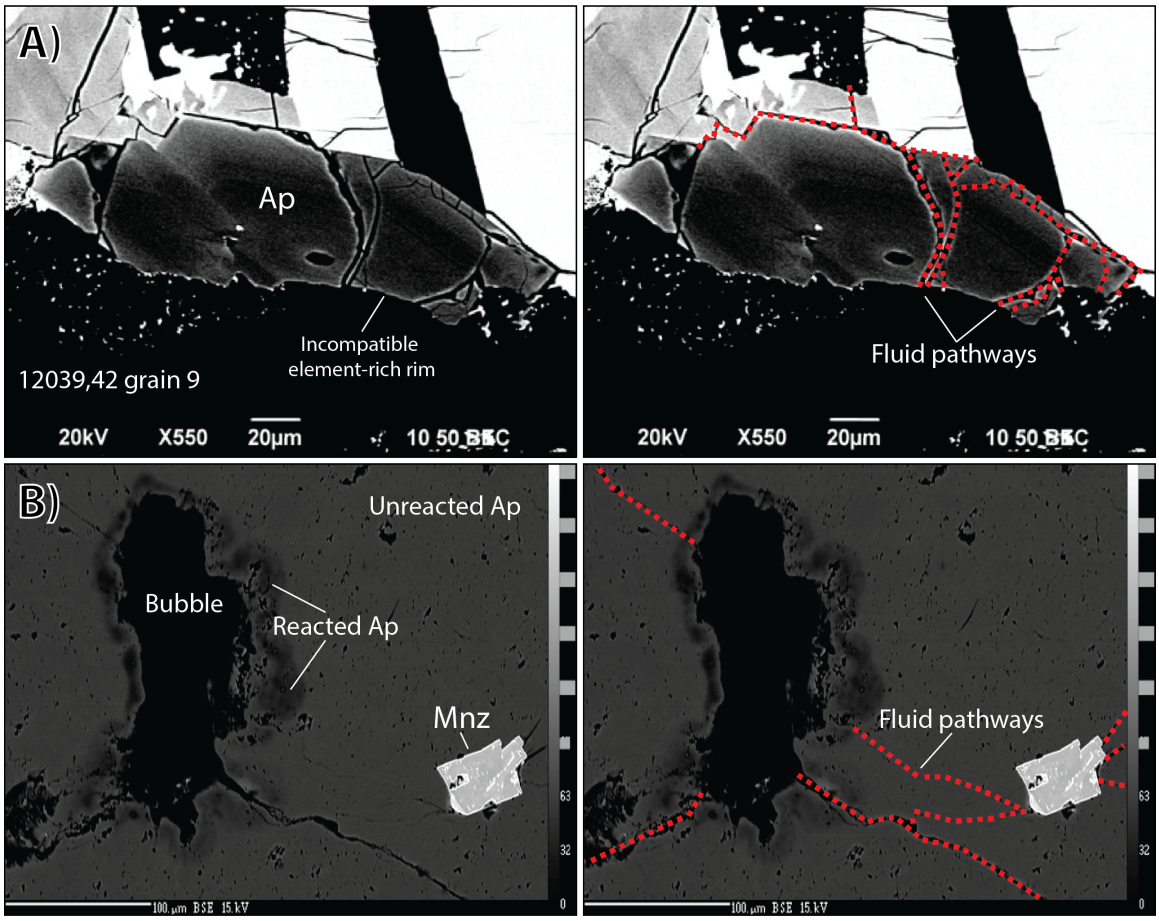

Figure DR3.

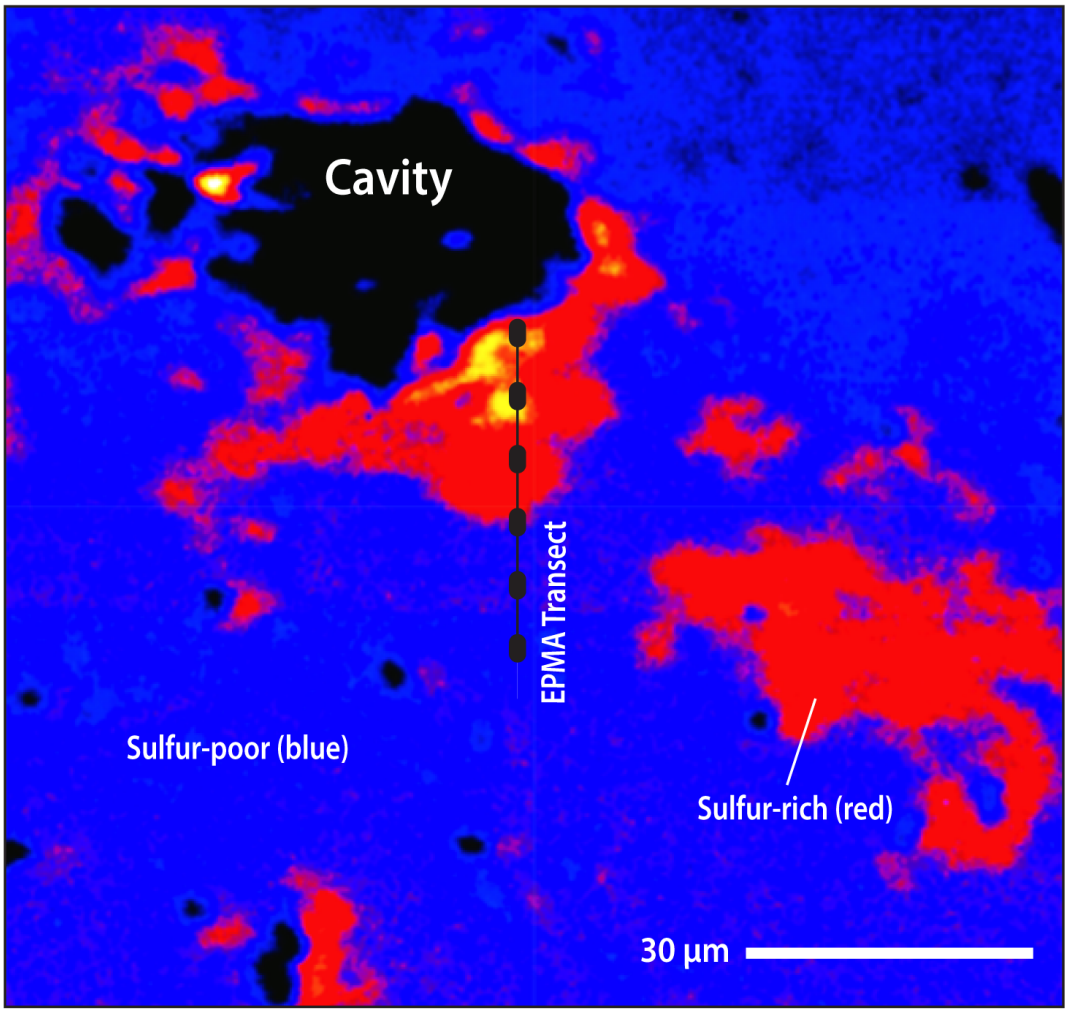

Data Repository Figures captions

Figure DR1 A-B: Volatile element zonation in lunar (sample 12039,42 grain 12 from Boyce et al., 2014) and terrestrial (Mina Carmen; this study) apatite. Both apatite samples show a systematic increase in S and Cl, and decrease in F, from core to rim (lunar) and proximity to a (formerly) volatile bearing cavities (terrestrial; see Figure 2B). Greenwood et al. (2011) reported S contents of the apatite core as below their (unpublished) limit of detection (l.o.d); we calculated a limit of detection of <200 μg/g S based on their reported analytical conditions (solid gray line). Symbols: Square: Mina Carmen apatite (IOA deposit, Chile); circles: lunar apatite data (Greenwood et al., 2011); semi-filled circle/square below limit of detection for S: ~30 μg/g S (solid gray line; Mina Carmen) and <200 μg/g S (solid gray line); open circles: data excluded by Boyce et al. (2014; see DR Section 3.1). Errors bars: 2σ (some smaller than symbol size).

Figure DR2 A-B: **Images of terrestrial and lunar apatite.** (A) High-contrast backscattered electron (BSE) images of lunar sample 12039,42 apatite grain 9 (note: different apatite grain than in Figure 1; BSE image modified from Greenwood et al., 2011). (B) BSE image of Mina Carmen apatite; scale bar in (B) is 100 μm. The potential volatile pathways (Nadeau et al., 2010; red dotted lines) that crosscut the apatite grain in (A) and radiate from the fluid/vapor cavity in (B) coupled with, incompatible element enriched apatite rims (A) and the presence of monazite (Mnz) inclusions (B; Harlov, 2015) infer volatile-induced metasomatic alteration of apatite.

Figure DR3: **X-ray fluorescence (XRF) map of apatite from Mina Carmen** (Treloar and Colley, 1996). The F-Cl-S contents measured along the EPMA transect are reported in DR Figure 1B and DR Table 2.4. The appearance of the map is biased by the 45^{o} angle of the incoming beam; i.e., areas on the right side of the cavity appear overexposed. Scale bar represents 30 μm.

Acknowledgments

This research used resources of the Advanced Photon Source, a U.S. Department of Energy (DOE) Office of Science User Facility operated for the DOE Office of Science by Argonne National Laboratory under Contract No. DE-AC02-06CH11357.